Rapid Nucleation and Slow Crystal Growth of CsPbI₃ Films Aided by Solvent Molecular Sieve for Perovskite Photovoltaics

Kai-Li Wang, Zhen-Huang Su, Yan-Hui Lou, Qiang Lv, Jing Chen, Yi-Ran Shi, Chun-Hao Chen, Yu-Hang Zhou, Xing-Yu Gao, Zhao-Kui Wang,* and Liang-Sheng Liao

The main reason for large energy loss in all-inorganic perovskites is ascribed to the slow nucleation and fast crystallization of all-inorganic perovskite films. Herein, a manipulating strategy is demonstrated to simultaneously realize rapid nucleation and slow crystal growth of CsPbI₃ perovskite films by employing solvent molecular sieves in the antisolvent. First, the antisolvent treatment of mixed chlorobenzene and ethyl alcohol can induce the instantaneous supersaturation of perovskites to achieve rapid nucleation. Subsequently, the molecular layer of phthalimide (2-N) molecules on the perovskite surface can be used as solvent molecular sieves to precisely control the evaporation of the solvent through molecule–solvent interactions. In addition, the molecules remaining on the surface can also effectively passivate the surface defects and improve the device performance. By this strategy, a synchronous regulation of rapid nucleation and slow crystal growth of perovskite films is realized for the first time. As a result, the CsPbI₃ film with 2-N treatment presents high-quality crystallinity with large grains and less defects. The champion device exhibits an outdoor power conversion efficiency (PCE) up to 20.14% under AM1.5G illumination, and an indoor PCE up to 40.07% (P_out:133.9 μW cm⁻²) under a commonly used light-emitting diode light source (2956 K, 1062 lux).

1. Introduction

Compared with organic–inorganic hybrid perovskites, all-inorganic (CsPbX₃) perovskites have excellent photothermic stabilities, which enables them have a good prospect in photovoltaic application. However, the fast crystallization rate of all-inorganic perovskites always induces the generation of many defects, which will cause large energy loss and seriously limit further improvement of their power conversion efficiency (PCE).[1,2] Therefore, how to slow down the crystallization rate of all-inorganic perovskite film with high-quality crystallinity is very important for further development of all-inorganic perovskite solar cells. In previous reports, the solvent engineering especially the antisolvent manipulation is considered as the effective methods to accurately control the crystallization process of all-inorganic perovskite thin films. For example, Yu et al. modified CsPbI₃ polycrystalline films with urea ammonium thiocyanate molten salt by fully releasing the coordination activity of SCN⁻ to achieve high-quality CsPbI₃ polycrystalline films.[3] Wang et al. demonstrated secondarily grown CsPbI₃ polycrystalline films with less defects by using the solid-state reaction between bromide and defects.[4] Yoon et al. also reported high-quality CsPbI₃ films prepared by controlling the middle stage of crystallization process through sequential drip of methyl ammonium chloride (MACl) solution (SDMs).[5] Very recently, Tan et al. used phenyltrimethylammonium iodide (PTAI) to improve the crystallization of CsPbI₃ polycrystalline films by effectively passivating defects.[6] Obviously, precise regulation of perovskite crystal growth is the key to obtain high-quality all-inorganic perovskite films, and a deep understanding of crystal growth kinetics is necessary.

In general, the growth of perovskite crystals can be divided into two processes: nucleation and growth of the grains.[7] Ummadisingu et al. summarized the morphological control of perovskite films, and systematically interpreted it as including volume free energy ($\Delta G_V = \gamma_s V$) and interfacial free energy ($\Delta G_S = \gamma_s A_s$). That is, the grain growth of perovskite film must overcome the Gibbs energy barrier and exceed the

K.-L. Wang, Q. Lv, J. Chen, Y.-R. Shi, C.-H. Chen, Y.-H. Zhou, Z.-K. Wang, L.-S. Liao
Institute of Functional Nano & Soft Materials (FUNSOM)
Jiangsu Key Laboratory for Carbon-Based Functional Materials & Devices
Soochow University
Suzhou 215123, P. R. China
E-mail: zkwang@suda.edu.cn

Z.-H. Su, X.-Y. Gao
Shanghai Synchrotron Radiation Facility
Shanghai Advanced Research Institute
Shanghai Institute of Applied Physics
Chinese Academy of Sciences
Shanghai 201204, P. R. China

Y.-H. Lou
College of Energy
Soochow Institute for Energy and Materials Innovations
Soochow University
Suzhou 215006, P. R. China

critical radius r^*.[8] Liu et al. deeply investigated the nucleation and crystal growth of perovskite films, including Lamer and Ostwald ripening models, and clearly pointed out that rapid nucleation followed by a slow crystal growth is essential in the formation of high-quality perovskite films.[9]

In recent years, a variety of methods have been developed to regulate the crystallization process of perovskite films, including component engineering, solvent strategy, antisolvent treatment, and interface modification.[10–14] Cheng et al. developed the rapid nucleation method for perovskite films by using chlorobenzene antisolvent during spin-coating.[15] Based on this strategy, some other antisolvent substitutes (toluene and chloroform, etc.) and their effects on the crystallization process of perovskites have also been reported.[16–20] However, most of these strategies can only achieve a single rapid nucleation or slow crystal growth process. There are few reports on the simultaneous regulation of rapid nucleation and slow crystal growth of perovskite films. Therefore, it is urgent to develop a new crystallization regulation strategy to realize the synchronous control of rapid nucleation and slow crystal growth, with a propose of fabricating highly efficient all-inorganic perovskite solar cells (PSCs).

Herein, a series of small molecules named as 1,3-indanedione (2-C), 1,2-benzenedicarboxylic anhydride (2-O), and phthalimide (2-N) were employed as antisolvent additives to treat the perovskite films during spin coating. These molecules could regulate the solvent evaporation and slow down the crystal growth rate of perovskite films. Combined with the antisolvent treatment method, this strategy realized the synchronous regulation of rapid nucleation and slow crystal growth of inorganic perovskite films. Based on this strategy, the optimized $CsPbI_3$ films exhibited high crystallinity with large grains and few defects. The fabricated device presented an outdoor PCE of 20.14% under AM 1.5G illumination and an indoor PCE of 40.07% under 1062 lux, respectively.

2. Results and Discussion

To realize the precise regulation of crystallization process of perovskite film, rapid nucleation, and slow crystal growth processes should be met at the same time. The antisolvent strategy has been proven to effectively induce the instantaneous supersaturation of perovskite precursor solution and realize the rapid nucleation of perovskite.[15–20] As shown in **Figure 1**a, we introduced a series of organic small molecules (2-C, 2-O, and 2-N) with similar structure into the antisolvent to treat perovskite
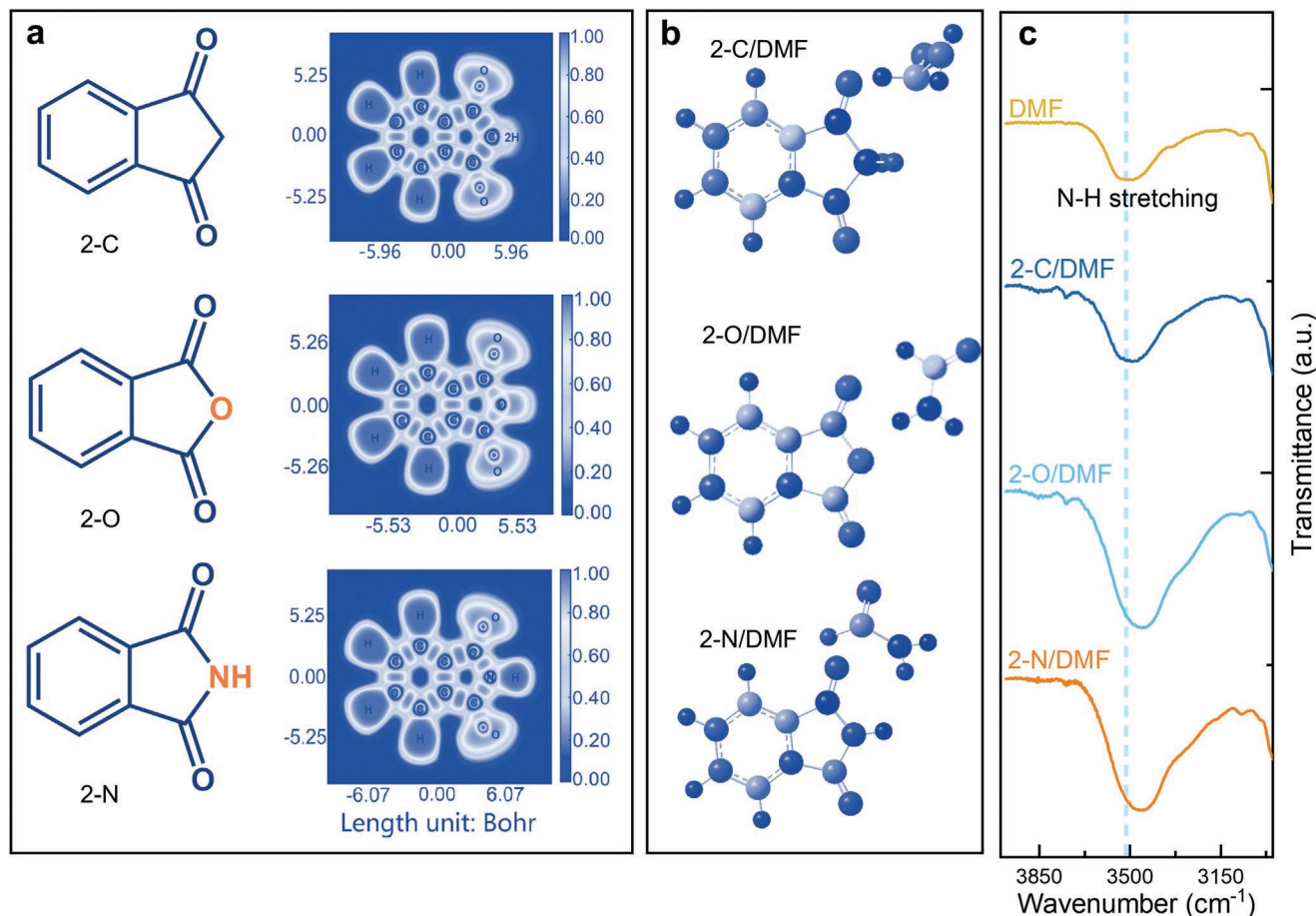
Figure 1. The interaction between molecules and solvents. a) The molecular structures (left) of 2-C, 2-O, and 2-N and the corresponding electron localization function (right) for molecules. b) The geometry optimization and Milliken charge distribution performance by using the DFT method. c) FTIR spectrum of solvents, including pure DMF, 2-C/DMF, 2-O/DMF, and 2-N/DMF solution.

**ADVANCED
SCIENCE NEWS**

www.advancedsciencenews.com

**ADVANCED
ENERGY
MATERIALS**

www.advenergymat.de

films during spin coating (Figure S1, Supporting Information). The double C=O group in the molecules has a strong interaction with the solvent, which can broaden the processing window and slow down the crystal growth process of perovskite films.[21,22] Furthermore, the incorporation of different groups (−C−, −O−, and −N−) is used to adjust the interaction and/or passivate the defects. The electron localization functions (ELF) of three molecules were used to evaluate their electronic properties and the interaction between molecules and solvent (Figure 1a), corresponding original color and partial enlarged images are shown in Figure S2 (Supporting Information). ELF is a 3D real-space function with values ranging from 0 to 1. In short, in the area surrounded by the isosurface of the ELF with a higher value, the electrons are more localized and not easy to run out. In contrast, electrons can easily move freely in such a region. Different groups did not significantly affect the electron localization distribution of adjacent C=O, suggesting that the functionality of these groups was only limited to themselves. Furthermore, the values of −N− region is significantly stronger than the −C− and −O− in the other molecules, indicating the electron localization of −N− group is significantly stronger than the −C− and −O− groups. That is, it could facilitate the interaction of molecules with solvent molecules or ions.[22–24]

To further quantify the interactions, density function theory (DFT) calculation was performed to evaluate the interaction energy (E_{ads}) between molecules (2-C, 2-O, 2-N) and the solvent (DMF). As shown in Figure 1b and Figure S3 (Supporting Information), the hydrogen bond between the solvent and molecules were characterized by stable geometric structure and minimizing the local energy of DMF and molecular complexes. The interaction energy (E_{ads}) is defined as the difference between the energy of the binary system and the sum of the energies of all molecules. The interaction energy of 2-N/DMF reached 43.49 kcal mol^{-1}, which was much higher than 17.53 kcal mol^{-1} for 2-C/DMF and 29.86 kcal mol^{-1} for 2-O/DMF. This result shows that 2-N treatment can maximize the process window and delay the growth of perovskite crystals. Furthermore, Fourier-transforms infrared spectrometer (FTIR) was carried out to verify the interaction between the molecules and solvent. Figure 1c and Figure S4 (Supporting Information) show the FTIR spectra of pure DMF, 2-C/DMF, 2-O/DMF, and 2-N/DMF solutions. Evidently, the stretching vibration of N-H appearing at 3506 cm^{-1} in the bare DMF solution[25] was shifted to 3495 cm^{-1}, 3464 cm^{-1} and 3443 cm^{-1} for 2-C/DMF, 2-O/DMF, and 2-N/DMF solutions, respectively. The decreased N–H stretching frequency indicates a reduction of force constant due to the decrease of bond strength between N and H after adduct formation.[20] And the lowest N−H stretching frequency in 2-N/DMF sample indicates the strongest interaction between 2-N and DMF molecules. Here, samples with or without 2-N molecules were selected for further study in subsequent work.

To evaluate the effect of 2-N molecule addition on perovskite nucleation and crystal growth process, further characterizations were conducted.

Firstly, to explore the underlying nucleation and crystal growth process mechanism, in situ absorption spectra of perovskite films (pristine, with CB/EtOH and CB/EtOH/2-N) during the thermal annealing process were tested. As shown in Figure S5 (Supporting Information), the spectrum of perovskite film with

CB/EtOH/2-N exhibited stronger absorption intensity, which means CB/EtOH/2-N treatment can improve the crystallinity of CsPbI$_3$ polycrystalline films. Furthermore, the variation of peak intensity ($I_{increase}$) at 700 nm with time (t) was used to track the crystallinity changes during the annealing treatment, this absorbance corresponds to the number and size of perovskite crystals in the film.[26,27] As shown in **Figure 2**a, the crystallization crystal of pristine film starts from a relatively slow nucleation process (0–2 min), followed by a rapid growth process (2–5 min), and the corresponding rates are $n_{pn} = 0.006$ and $n_{pc} = 0.14$, respectively.[27] In contrast, in the CB/EtOH and CB/EtOH/2-N-based films, the nucleation process was hardly observed, indicating that the films had entered the crystal growth stage during the antisolvent treatment. Furthermore, the crystal growth rate of the CB/EtOH-based films ($n_{pc} = 0.11$) was close to that of the pristine films, indicating that a single antisolvent treatment hardly affects the crystal growth rate. The CB/EtOH/2-N-treated perovskite films ($n_{pc} = 0.07$) exhibited a significantly slower crystal growth rate in all samples, indicating that the introduction of 2-N molecules effectively delayed the crystal growth process. Overall, antisolvent treatment (CB/EtOH) can accelerate the nucleation process, while the introduction of 2-N molecules can effectively retard the crystal growth process and improve the quality of CsPbI$_3$-based polycrystalline films.

To understand the effect of antisolvent treatment on the perovskite film crystallization process, in situ optical microscopy was used to monitor the CsPbI$_3$ precursor polycrystalline films with various treatment as shown in Figure 2b. Corresponding videos were recorded in Figure S6 (Supporting Information). We monitored the crystallization process of perovskite films in real time by dropping antisolvent on the spin-coated perovskite films and tracking the spread tracks. Until 5 min, no obvious perovskite seeds were observed in the CsPbI$_3$ polycrystalline film without any treatment. In contrast, the perovskite seeds were formed at the moment of antisolvent dropping in the antisolvent treated samples regardless of incorporating 2-N molecules or not. This means that antisolvent (with or without 2-N) treatment can directly induce the formation of perovskite seeds while largely eliminating the slow nucleation process. In addition, with increasing the time of antisolvent treatment, the number and volume of perovskite seeds also increased significantly. Meanwhile, it could be found that the antisolvent treated film turned into a coffee color containing crystal nucleus (Figure S7, Supporting Information), whereas the pristine film was almost transparent light yellow. Interestingly, the introduction of 2-N molecules had a negligible effect on the perovskite seeds growth rate of CsPbI$_3$ perovskite polycrystalline films. We ascribed it to the dominant role of a large number of antisolvents, compared with a small number of 2-N molecules. Undeniably, the introduction of 2-N molecules into antisolvent treatment still effectively induced the rapid perovskite seeds of perovskite compared with the untreated sample. To explore the effect of the introduction of molecules (2-C, 2-O, and 2-N) on the solvent volatilization process, which is related to the crystal growth process of perovskite films. In situ contact angle measurement was employed to evaluate the solvent evaporation during the annealing process (Figure 2c and Figure S8, Supporting Information). In this process, CB/EtOH (100 μL), 2-C,
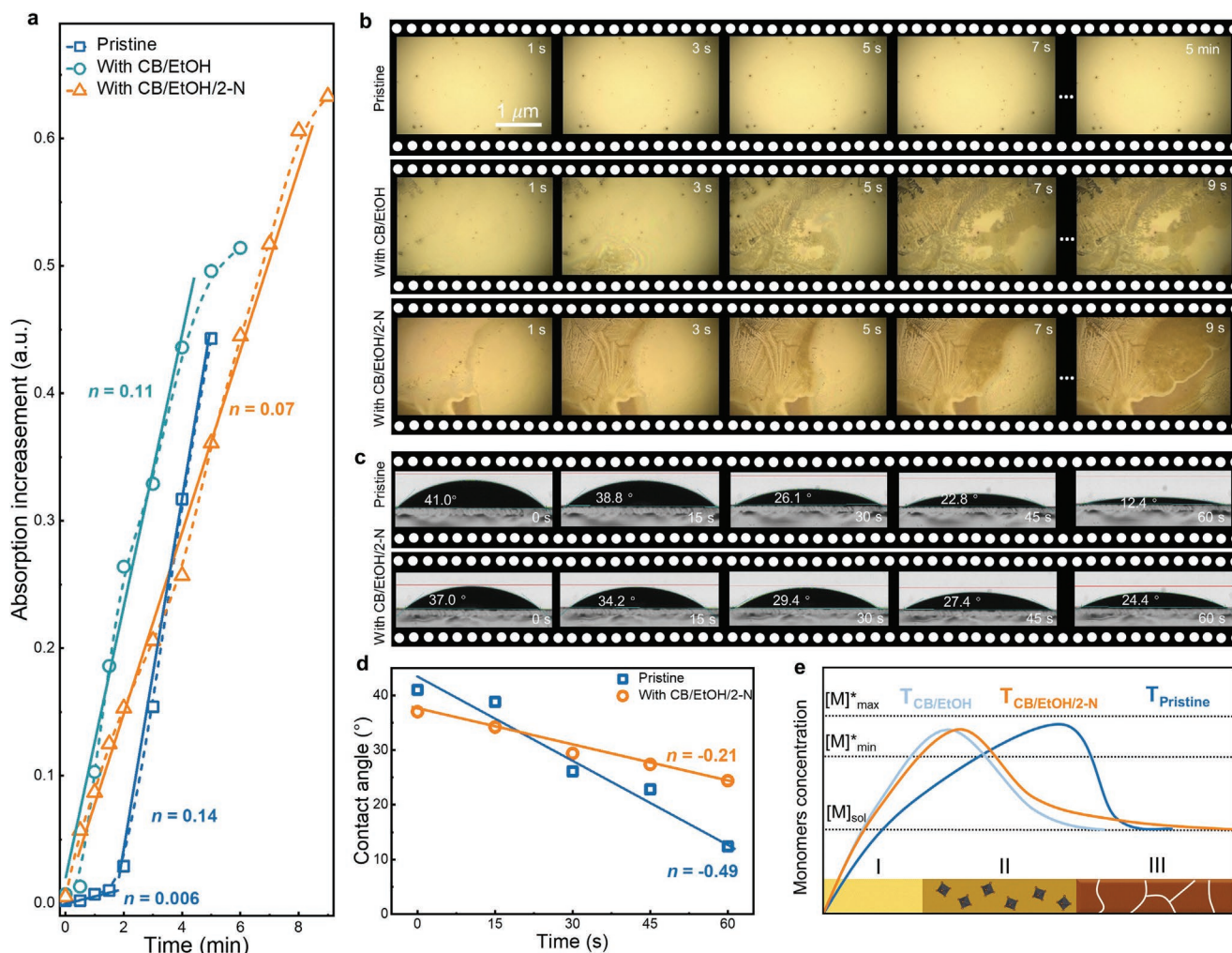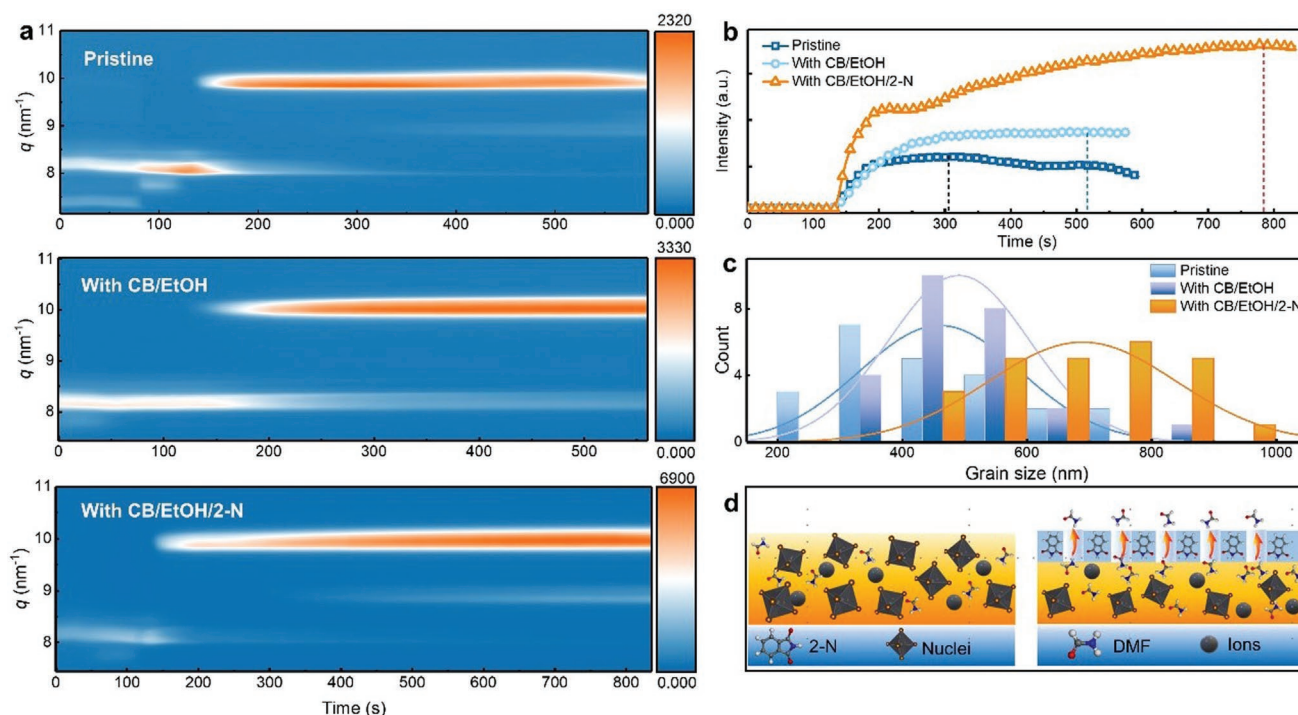
Figure 2. The crystallization process of perovskite films. a) The evolution of absorption intensity at 700 nm of the perovskite film and with different treatments. All the films to be thermally annealed were heated at 210 °C under humid air conditions (RH ≈ 10%). b) The in situ optical microscopy images of perovskite films without any treatment, with CB/EtOH treatment or with 2-N treatment. The in situ contact angle of perovskite solution c) without or with 2-N additive at 210 °C. d) Time-dependent contact angle change. e) The LaMer diagram of nucleation and growth dynamics for different perovskite films.

2-O, and 2-N (1.5 mg mL^{-1}) were added to the perovskite precursor solution and heated at 210 °C to simulate the annealing process. Figure 2d and Figure S9 (Supporting Information) plot the fitting diagram of measured contact angles as a function of time. Obviously, the 2-N based sample exhibited a slowest decreases rate ($n = -0.21$), compared with pristine ($n = -0.49$), CB/EtOH ($n = -0.45$), 2-C ($n = -0.39$), and 2-O ($n = -0.28$) samples. After adding 2-N, the decay rate of contact angle was slow, corresponding to a slow evaporation rate for the solvent. In other words, the introduction of 2-N could effectively slow down the crystal growth of perovskite films.

The overall nucleation and crystal growth process of perovskite can be depicted by the LaMer graph, which describes the change of the perovskite precursor concentration as at a constant and isothermal evaporation rate of solvent. LaMer diagram is divided into three stages: prenucleation (I), nucleation (II), and crystal growth stage (III).[9] When the monomer concentration is lower than the critical supersaturation value ($[M]_{min}$),

the nucleation will be terminated. When the monomer concentration decreases below the solubility value ($[M]_{sol}$), the crystal growth will be finally completed.[28,29] Combined with the present case, we draw a LaMer graph as shown in Figure 2e. the introduction of 2-N hardly affects the rapid nucleation rate of perovskite, but it can significantly slow down the crystal growth of perovskites. Noticeably, 2-N molecules can act as a solvent molecular sieve to accurately control the evaporation of solvent since they are mainly distributed on the surface of perovskite film.

In situ grazing-incidence wide-angle X-ray scattering (GIWAXS) was employed to track the effect of molecular additives on the crystal growth process of perovskite films including those of the pristine film and treated films by CB/EtOH with and without 2-C, 2-O, and 2-N molecules (Figures S10 and S11, Supporting Information). **Figure 3**a selectively shows the 2-D GIWAXS spectra of the (110) peak of pristine film, film with CB/EtOH, and film with 2-N, as a function of time. The

Figure 3. In situ GIWAXS monitoring the crystal growth process of perovskite films. a) Top view image of $CsPbI_3$ (110) peak in GIWAXS images. b) Corresponding variations in the (110) peak intensity with time during $CsPbI_3$ film growth under annealing conditions. c) The grain size distribution of pristine, with CB/EtOH and with 2-N perovskite films. d) The schematic diagram of the slowed down perovskite crystal growth process with 2-N molecule.

pristine perovskite film showed a narrow process window, and the intensity of (110) peak began to decay significantly at 500 s. In contrast, the film treated with antisolvent of CB/EtOH presented excellent crystal growth process, regardless of whether 2-N molecules were added to the antisolvent. Especially for the case of incorporating 2-N molecules, the process window of perovskite film was significantly widened, and the intensity of (110) peak was also significantly improved. Figure 3b summarized the fluctuation of peak intensity of (110) peak in three samples with annealing time. The position of (110) peaks appearing was moved to the same for further comparison. The optimum crystallization time of pristine films is about 300 s, which is consistent with previous reports.[30,31] The optimal crystallization time and the peak strength of CB/EtOH-based film were largely improved, indicating that the anti-solvent treatment could effectively induce a rapid nucleation of $CsPbI_3$ polycrystalline film. Particularly, the optimum crystallization time of 2-N treated film reached an amazing 780 s, and the (110) peak intensity was obviously higher than other samples, proving that the 2-N molecules could effectively slow down the crystal growth process and further improved the crystallinity of $CsPbI_3$ polycrystalline film. The morphologies of perovskite films with different treatments were further evaluated by scanning electron microscopy (Figure S12, Supporting Information). Figure 3c shows the grain size statistics of three samples. The average grain size of 2-N treated perovskite film was significantly enlarged to 689 nm, compared with pristine (460 nm) and CB/EtOH (491 nm) treated films. The good film morphology with large grains proves that the introduction of 2-N molecules can effectively improve the quality of $CsPbI_3$

polycrystalline films. In order to describe the role of 2-N molecules, a schematic diagram of perovskite crystal growth is drawn in Figure 3d. After the rapid nucleation induced by antisolvent treatment, the perovskite film entered the III stage of crystal growth. Meanwhile, the 2-N molecular layer played a role of solvent molecular sieve on the perovskite surface in alleviating the evaporation process of solvent through forming strong interaction with the solvent. This process could effectively slow down the growth process of perovskite crystals and obtain high-quality perovskite films with large grains. Furthermore, the spatial positions of 2-N molecules on the perovskite films were monitored by energy-dispersive X-ray (EDX) and time-of-flight secondary-ion mass spectrometry (TOF-SIMS) spectra. As shown in Figure S13 (Supporting Information), O and N (labeled 2-N) were uniformly distributed on the perovskite film like Pb, I, and Cs elements. Meanwhile, we also found that the 2-N molecules are mainly distributed on the perovskite surface from TOF-SIMS spectrum (Figure S14, Supporting Information). To this end, 2-N molecules uniformly distributed on the surface of the perovskite films are like solvent molecular sieves, controlling the volatilization of the solvent through strong interactions.

The trap states of perovskite films with and without 2-N were further investigated by thermal admittance spectroscopy and drive-level capacitance profiling (DCLP) techniques. As shown in **Figure 4**a, the trap density of 2-N treated perovskite film was obviously reduced in the shallow region (0.25–0.45 eV). Furthermore, DLCP characterization was applied to determine the spatial distribution of defects in the perovskite films (Figure 4b). An obvious reduction of the trap density along
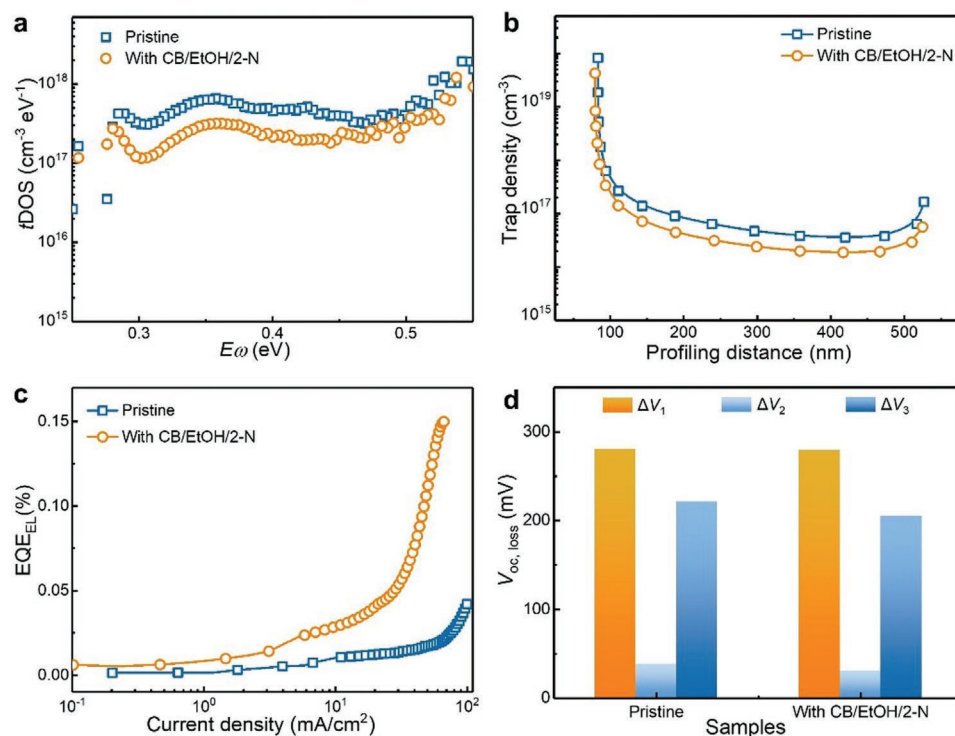
Figure 4. Defect distribution and device energy loss before and after 2-N treatment. a) The energy-dependent trap density of states (*t*DOS) of solar cells with and without 2-N treated, measured by the thermal admittance spectroscopy (TAS) method. b) The dependence of trap density on profiling distance of the pristine and 2-N-based devices. c) EQE$_{EL}$ of the reference and target PIPVs. d) The V_{oc} loss analysis of the reference and target PSCs.

the profiling distance in the whole perovskite film was also observed. Both reductions of the trap states in the energetic and spatial distributions indicate that a high-quality perovskite film was obtained after 2-N treatment. Generally, lower trap state means better photovoltaic performance of corresponding devices. The characterization of electrochemical impedance (EIS) spectroscopy (Figure S15, Supporting Information) demonstrated that 2-N treated device presented lower sheet resistance (R_{sh}) compared with the pristine device, implying a substantial suppressed recombination and a smaller voltage loss (ΔV).[32–35]

In general, ΔV can be quantitatively defined by $q\Delta V = q(\Delta V_1 + \Delta V_2 + \Delta V_3)$, where q is the elementary charge, ΔV_1 is associated with the nonradiative recombination above the bandgap, ΔV_2 is from the blackbody radiation, and ΔV_3 is from the nonradiative recombination.[36,37] From the bandgaps of perovskite films with or without 2-N (Figure S16, Supporting Information), both samples had similar ΔV_1 values of 279.40 and 280.67 mV, respectively. From the highly sensitive EQE measurement (Figure S17, Supporting Information), the ΔV_2 values were determined to be 38.32 and 30.29 mV for pristine and 2-N based devices, respectively. The ΔV_3 can be expressed by the equation of $\Delta V_3 = \frac{k_B}{q}\ln(EQE_{EL})$, where the EQE$_{EL}$ value can be collected by using the devices as a light-emitting diode as shown in Figure 4c. From the EQE$_{EL}$, the ΔV_3 values were calculated to be 221.05 and 205.13 mV for the control device and the target device, respectively. Figure 4d plots the voltage loss including ΔV_1, ΔV_2, and ΔV_3 in both devices. Obviously,

2-N treated device presented lower voltage loss especially for ΔV_2 and ΔV_3, which are consistent with the EIS analysis.

Finally, planar structure perovskite solar cells with a configuration of FTO/TiO$_2$/CsPbI$_3$/Spiro-OMeTAD/MoO$_3$/Ag were fabricated to verify the positive role of 2-N additive in the photovoltaic performance. Figure S18 (Supporting Information) exhibited the cross-sectional scanning electron microscopy (SEM) of devices based on the perovskite films with or without CB/EtOH/2-N treatment, the larger grain size and denser perovskite films demonstrate the positive effect of 2-N. As shown in **Figure 5**a and Figure S19 and Table S1 (Supporting Information), the control device exhibited a PCE of 17.24% with short-circuit current density (J_{sc}) of 20.47 mA cm^{-2}, a V_{oc} of 1.09 V, and a fill factor (FF) of 0.78. In contrast, the target device presented a significantly improved PCE of 20.14% with a J_{sc} of 20.91 mA cm^{-2}, a V_{oc} of 1.19 V, and an FF of 0.81. Figure 5b plots the histograms of PCE and V_{oc} distributions of the control and the target devices. It indicates that the excellent repeatability and efficiency of the target device were mainly relied on the improvement of V_{oc}. The external quantum efficiency (EQE) of the target devices as shown in Figure 5c was over 93% with an integrated current density of 20.01 mA cm^{-2}, which is closed to the value from the current density–voltage (J–V) curve. As a comparison, the integral current of the pristine device from the EQE spectrum is only 19.58 mA cm^{-2}. In addition, CsPbI$_3$ perovskites are regarded as a suitable representative for indoor photovoltaic application by their matching absorption spectra with the artificial light source.[38–43] Therefore, we further characterized the indoor performance of the control and the target devices under
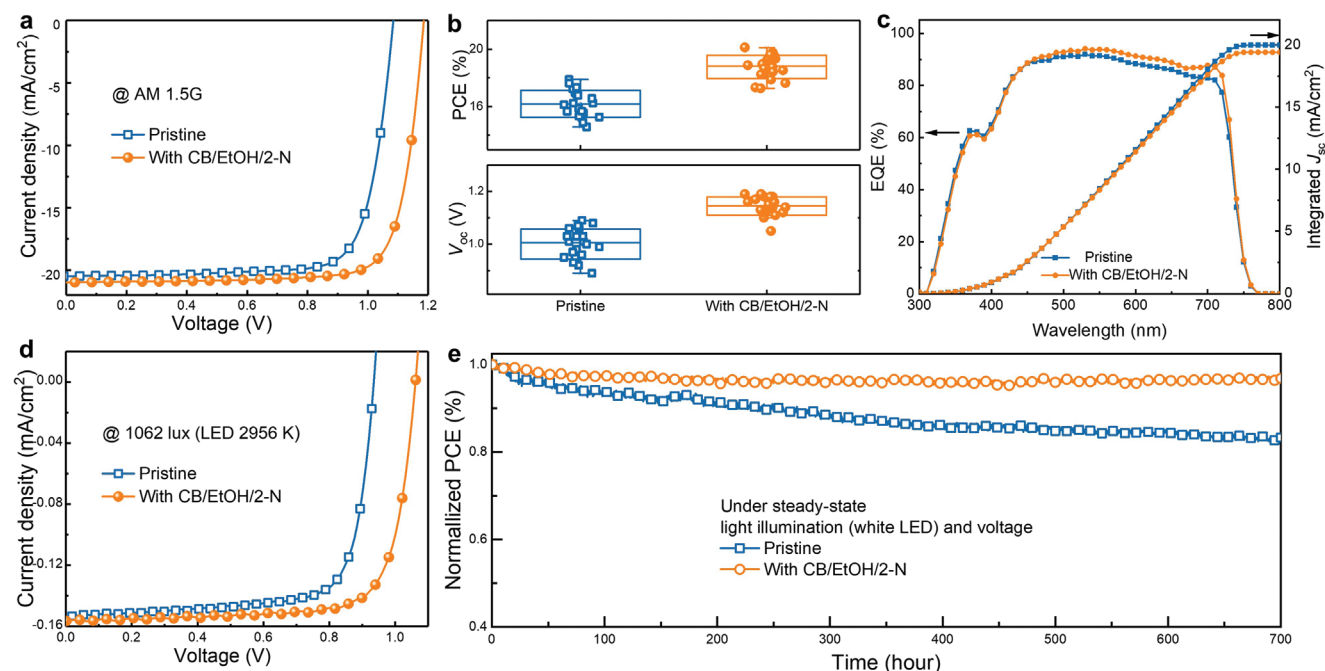
Figure 5. The performance of devices with or without 2-N treatment. a) J–V curves of the pristine and 2-N-based PSCs under simulated AM 1.5G solar illumination. b) The PCE and V_{oc} distribution of pristine and 2-N-based devices. c) EQE of 2-N-based devices. d) J–V curves of the pristine and 2-N-based PSCs under indoor light (LED 2956 K@1062 lux) conditions. e) PCE tracking of the devices over 700 h under a continuous white LED light illumination (N_2 glove box).

indoor light sources (2956 K@1062 lux). As shown in Figure 5d and Figure S20 and Table S2 (Supporting Information), the target device delivered a significant improved PCE from 32.88% to a 40.07% compared with the control device.

The prominent enhancement of PCE was also mainly attributed to the increases of V_{oc} (from 0.97 to 1.06 V) and FF (from 0.75 to 0.82). Generally, nonradiative recombination of carrier mediated by defects and traps under indoor low-light condition has greater lethality to the indoor photovoltaic performance, we ascribed the largely improved indoor PCE to the high-quality $CsPbI_3$ perovskite polycrystalline films with less defects as aforementioned. We also tested the device's operational stability under continuous light illumination and high-temperature conditions, which related to the stability of devices in real applications. As shown in Figure 5e, the target devices still maintain an initial efficiency of 93% after more than 700 h of continuous light (LED) illumination. As a control, the pristine device maintained only 80% of the initial efficiency. Meanwhile, the target device also can still retain 91% of the initial efficiency (77% for the pristine devices) after more than 500 h in a nitrogen environment at 85 °C (Figure S21, Supporting Information). Considering that all-inorganic devices are sensitive to moisture, the stability of the devices in humid air was also tested. As shown in Figure S22 (Supporting Information), the target devices also exhibited excellent operational stability retaining 87% of the original PCE value after 700 h of aging under the atmosphere (RH <20%, 20–25 °C). In contrast, the PCE of the control devices rapidly dropped to 63% of the initial value within the same time aging. We explain that the higher quality and better hydrophobicity (Figure S23, Supporting Information) of CB/EtOH/2-N-based perovskite films can effectively improve

device stability.[44–47] In addition, these results indicated that our developed solvent molecular sieve strategy for manipulating the crystallization of $CsPbI_3$ perovskites could guarantee the promising device performance of all-inorganic PSCs.

3. Conclusions

In summary, we have demonstrated a solvent molecular sieve strategy to achieve crystal growth regulation including rapid nucleation and slow crystal growth by using 2-N-based organic small molecules as the antisolvent additives. The molecular thin layer of organic small molecules could act as a solvent molecular sieve to regulate the evaporation process of solvent during the annealing process and slow down the crystal growth rate of perovskite films owing to their strong interaction with the solvent. The developed strategy realized a synchronous regulation of rapid nucleation and slow crystallization of perovskite films for the first time. The high-quality $CsPbI_3$ polycrystalline films with large grains and less defects enable the devices delivered an outdoor PCE of 20.14% under AM1.5G illumination and an indoor PCE of 40.07% under 1062 lux irradiation. The finding in this work provides an effective route to prepare high-quality all-inorganic perovskite films for indoor and outdoor photovoltaic applications.

4. Experimental Section

Materials and Methods: Lead iodide (PbI_2, 99.999%), barium iodide (CsI, 99.99%), chlorobenzene (CB), ethyl alcohol (EtOH), and N,N-dimethylformamide (DMF, 99.9%) were purchased from Alfa Aesar Ltd.

Dimethylammonium iodine (DMAI, 99.99%) was purchased from TCI Corporation. Spiro-OMeTAD, Ag (99.999%), and MoO_3 were purchased from Advanced Election Technology Co., Ltd. Sulfonyl imide (Li-TFSI) and TBP were purchased from 1-Material Ltd. 1,3-Indanedione (2-C), 1,2-benzenedicarboxylic anhydride (2-O), and phthalimide (2-N) were purchased from 1-Material Ltd.

DFT Calculations: All DFT calculations were performed using Gaussian 09. Gauss View 5.0 was used to construct initial structures used in computations. The initial structure was optimized with the DFT density functional and the 6-311G, the optimized geometries were verified by frequency calculations as minima (zero imaginary frequencies) at the same level of theory as that used for geometry optimization.

Device Fabrication: All-inorganic PSCs were fabricated with the following structure: $FTO/TiO_2/CsPbI_3/spiro-OMeTAD/MoO_3/Ag$. The FTO (15 Ω sq^{-1}) substrates were sequentially cleaned with deionized water, acetone, and ethanol in an ultrasonic bath for 15 min each. The cleaned FTO substrates were immersed into 200 mL $TiCl_4$ solution at 70 °C for 1 h. The perovskite precursor solution (CsI, PbI_2, and DMAI were dissolved in anhydrous DMF with the molar ratio of 1:1:1.2 to form a 0.7 M precursor solution) was spin-coated at 4500 rpm for 30 s. At 25 s, the substrate was treated with CB/EtOH (volume ratio is 1:1, with (1.5 mg mL^{-1}) or without molecules) drop-casting. The pristine, with CB/EtOH, with 2-C (1.5 mg mL^{-1}), with 2-O (1.5 mg mL^{-1}) and with 2-N (1.5 mg mL^{-1}) samples were annealed at 210 °C for 300, 330, 420, 480 and 540 s, respectively. Then, the spiro-OMeTAD (90 mg mL^{-1} in CB with 22.5 µL bis(trifluoromethane) sulfonamide lithium salt solution (520 mg mL^{-1} in acetonitrile), and 36 µL 4-tert-butylpyridine) was coated onto the perovskite layer at 5000 rpm for 40 s. Finally, the samples were transferred into a vacuum chamber for the deposition of MoO_3 layer (8 nm) and Ag electrode (100 nm) at a pressure $< 2 \times 10^{-6}$ Torr. Except that different the mask shapes were used, the effective area of each cell is 0.09 cm^2.

Device Characterization: *J–V* characteristics of $CsPbI_3$ PSCs (0.09 cm^2) were taken using a Keithley 2400 source meter under a simulated AM 1.5G spectrum at 100 mW cm^{-2}. In addition, the emission spectra and power intensity of LED indoor light source (Osram L18W/827) were carried out following a previous report measured by a high-precision fiber-optics spectrometer (Spectrilight ILT950) equipped with a cosine corrector (Ocean Optics, CC-3-UV-S). Then, thinner masks were used and did an antireflection treatment on it. In addition, the area of the aperture was decreased to 0.3 × 0.3 cm^2 which would be more suitable for the 0.4 × 0.4 cm^2 cells. All the devices were measured without preconditioning such as light-soaking and applied bias voltage. The standard *C–V*, DLCP, and TAS were tested by using an IM6e Electrochemical Workstation (ZAHNER, Germany), *C–f* was carried out on a precision impedance analyzer (Agilent 4294A).

Materials Characterization: Surface images of the films and cross-sectional image were acquired by scanning electron microscopy (SEM, Quanta 200 FEG.). In situ GIWAXS test was performed at the BL14B1 beamline of China Shanghai Synchrotron Radiation Facility (SSRF). The contact angles of the grid lines were measured by a PSSOCA20 optical contact-measuring system. The in situ microscopy images and fluorescence microscopy images were taken from an inverted fluorescence microscope (Leica, DM4000 M, Germany).

Supporting Information

Supporting Information is available from the Wiley Online Library or from the author.

Acknowledgements

Conflict of Interest

The authors declare no conflict of interest.

Data Availability Statement

The data that support the findings of this study are available from the corresponding author upon reasonable request.

[1] T. Liu, J. Ma, M. Qin, P. Li, L. Han, Y. Zhang, Y. Song, *Energy Environ. Sci.* **2022**, *15*, 413.

[2] Z. Gu, Z. Zhou, Z. Huang, K. Wang, Z. Cai, X. Hu, Y. Song, *Adv. Mater.* **2020**, *32*, 1908006.

[3] B. Yu, J. Shi, S. Tan, Y. Cui, W. Zhao, H. Wu, Q. Meng, *Angew. Chem., Int. Ed.* **2021**, *60*, 13436.

[4] X. Wang, Y. Wang, Y. Chen, X. Liu, Y. Zhao, *Adv. Mater.* **2021**, *33*, 2103688.

[5] J. Zhang, Y. Fang, W. Zhao, R. Han, J. Wen, S. Liu, *Adv. Mater.* **2021**, *33*, 2103770.

[6] S. Tan, B. Yu, Y. Cui, F. Meng, C. Huang, Y. Li, Q. B. Meng, *Angew. Chem.* **2022**, *134*, e202201300.

[7] C. Bi, Q. Wang, Y. Shao, Y. Yuan, Z. Xiao, J. S. Huang, *Nat. Commun.* **2015**, *6*, 7747.

[8] A. Ummadisingu, L. Steier, J. Y. Seo, T. Matsui, A. Abate, W. Tress, M. Grätzel, *Nature* **2017**, *545*, 208.

[9] C. Liu, Y. B. Cheng, Z. Ge, *Chem. Soc. Rev.* **2020**, *49*, 1653.

[10] Y. Zhou, M. Yang, W. Wu, A. L. Vasiliev, K. Zhu, N. P. Padture, *J. Mater. Chem. A* **2015**, *3*, 8178.

[11] C. Liu, K. Wang, P. Du, T. Meng, X. Yu, S. Z. Cheng, X. Gong, *ACS Appl. Mater. Interfaces* **2015**, *7*, 1153.

[12] N. Ahn, D. Y. Son, I. H. Jang, S. M. Kang, M. Choi, N. G. Park, *J. Am. Chem. Soc.* **2015**, *137*, 8696.

[13] M. Li, C. Zhao, Z. K. Wang, C. C. Zhang, H. Lee, A. Pockett, J. Barbé, W. C. Tsoi, Y. G. Yang, M. Carnie, X. Y. Gao, W. X. Yang, J. Durrant, L. S. Liao, S. Jain, *Adv. Energy Mater.* **2018**, *8*, 1801509.

[14] Z. Xiao, Q. Dong, C. Bi, Y. Shao, Y. Yuan, J. Huang, *Adv. Mater.* **2014**, *26*, 6503.

[15] M. Xiao, F. Huang, W. Huang, Y. Dkhissi, Y. Zhu, J. Etheridge, L. A. Spiccia, *Angew. Chem., Int. Ed.* **2014**, *53*, 9898.

[16] S. Paek, P. Schouwink, E. N. Athanasopoulou, K. T. Cho, G. Grancini, Y. Lee, P. Gao, *Chem. Mater.* **2017**, *29*, 3490.

[17] Y. Wang, J. Wu, P. Zhang, D. Liu, T. Zhang, L. Ji, S. Li, *Nano Energy* **2017**, *39*, 616.

[18] D. Gedamu, I. M. Asuo, D. Benetti, M. Basti, I. Ka, S. G. Cloutier, R. Nechache, *Sci. Rep.* **2018**, *8*, 12885.

[19] Y. H. Seo, E. C. Kim, S. P. Cho, S. S. Kim, S. I. Na, *Appl. Mater. Today* **2017**, *9*, 598.

[20] Q. Q. Ye, Z. K. Wang, M. Li, C. C. Zhang, K. H. Hu, L. S. Liao, *ACS Energy Lett.* **2018**, *3*, 875.

[21] M. A. Sattar, M. Javed, M. Benkraouda, N. Amrane, *Int. J. Energy Res.* **2021**, *45*, 4793.

[22] V. Maurya, K. B. Joshi, *J. Phys. Chem. A* **2019**, *123*, 1999.

[23] J. Navas, A. Sánchez-Coronilla, J. J. Gallardo, N. C. Hernández, J. C. Piñero, R. Alcántara, J. Martín-Calleja, *Nanoscale* **2015**, *7*, 6216.

[24] J. E. Katon, W. R. Feairheller, *Spectrochim. Acta* **1965**, *21*, 199.

[25] H. H. Huang, Q. H. Liu, H. Tsai, S. Shrestha, L. Y. Su, P. T. Chen, L. Wang, *Joule* **2021**, *5*, 958.

[26] Q. Liang, J. Liu, Z. Cheng, Y. Li, L. Chen, R. Zhang, Y. Han, *J. Mater. Chem. A* **2016**, *4*, 223.

[27] Y. Tidhar, E. Edri, H. Weissman, D. Zohar, G. Hodes, D. Cahen, B. Rybtchinski, S. Kirmayer, *J. Am. Chem. Soc.* **2014**, *136*, 13249.

[28] S. G. Kwon, T. Hyeon, *Small* **2011**, *7*, 2685.

[29] H. D. Kamaruddin, W. J. Koros, *J. Membr. Sci.* **1997**, *135*, 147.

[30] Y. Wang, X. Liu, T. Zhang, X. Wang, M. Kan, J. Shi, Y. Zhao, *Angew. Chem.* **2019**, *131*, 16844.

[31] Y. Wang, M. I. Dar, L. K. Ono, T. Zhang, M. Kan, Y. Li, Y. Zhao, *Science* **2019**, *365*, 591.

[32] C. C. Zhang, S. Yuan, Y. H. Lou, Q. W. Liu, M. Li, H. Okada, Z. K. Wang, *Adv. Mater.* **2020**, *32*, 2001479.

[33] R. Wang, J. J. Xue, K. L. Wang, Z. K. Wang, Y. Luo, D. Fenning, Y. Yang, *Science* **2019**, *366*, 1509.

[34] Y. Yang, Y. Luo, P. Guo, H. Sun, Y. Yao, *Phys. Rev. Appl.* **2017**, *7*, 044017.

[35] J. H. Xue, R. Wang, K. L. Wang, Z. K. Wang, I. Yavuz, Y. Wang, Y. Yang, *J. Am. Chem. Soc.* **2019**, *141*, 13948.

[36] F. Li, X. Deng, F. Qi, Z. Li, D. Liu, D. Shen, A. K. Y. Jen, *J. Am. Chem. Soc.* **2020**, *142*, 20134.

[37] C. Dong, X. M. Li, C. Ma, W. F. Yang, J. J. Cao, F. Igbari, Z. K. Wang, L. S. Liao, *Adv. Funct. Mater.* **2021**, *31*, 2011242.

[38] M. Freitag, J. Teuscher, Y. Saygili, X. Zhang, F. Giordano, P. Liska, A. Hagfeldt, *Nat. Photonics* **2017**, *11*, 372.

[39] K. L. Wang, X. M. Li, Y. H. Lou, M. Li, Z. K. Wang, *Sci. Bull.* **2021**, *66*, 347.

[40] D. Zheng, R. Peng, G. Wang, J. L. Logsdon, B. Wang, X. Hu, A. Facchetti, *Adv. Mater.* **2019**, *31*, 1903239.

[41] K. .L. Wang, Y. G. Yang, Y. H. Lou, M. Li, F. Igbari, J. J. Cao, Z. K. Wang, *eScience* **2021**, *1*, 53.

[42] K. L. Wang, Y. H. Zhou, Y. H. Lou, Z. K. Wang, *Chem. Sci.* **2021**, *12*, 11936.

[43] M. Li, F. Igbari, Z. K. Wang, L. S. Liao, *Adv. Energy Mater.* **2020**, *10*, 2000641.

[44] C. Li, Q. Guo, H. Zhang, Y. Bai, F. Wang, L. Liu, Z. A. Tan, *Nano Energy* **2017**, *40*, 248.

[45] T. Zhang, M. Long, K. Yan, M. Qin, X. Lu, X. Zeng, J. Xu, *Adv. Energy Mater.* **2017**, *7*, 1700118.

[46] J. Liang, Z. Liu, L. Qiu, Z. Hawash, L. Meng, Z. Wu, Y. Qi, *Adv. Energy Mater.* **2018**, *8*, 1800504.

[47] Q. Wali, F. J. Iftikhar, *Polyhedron* **2021**, *199*, 115089.